exoALMA. I. Science goals, project design, and data products

Teague, R.; Benisty, M.; Facchini, S.; Fukagawa, M.; Pinte, C.; Andrews, S.M.; ... ; Zawadzki, B.

CrossMark

exoALMA. I. Science Goals, Project Design, and Data Products

Richard Teague[1], Myriam Benisty[2,3], Stefano Facchini[4], Misato Fukagawa[5], Christophe Pinte[6,7], Sean M. Andrews[8], Jaehan Bae[9], Marcelo Barraza-Alfaro[1], Gianni Cataldi[10], Nicolás Cuello[6], Pietro Curone[4,11], Ian Czekala[12,13], Daniele Fasano[6,14], Mario Flock[3], Maria Galloway-Sprietsma[9], Himanshi Garg[7], Cassandra Hall[15,16,17], Iain Hammond[7], Thomas Hilder[17], Jane Huang[7,18], John D. Ilee[19], Andrés F. Izquierdo[20,21,33], Kazuhiro Kanagawa[22], Geoffroy Lesur[6], Giuseppe Lodato[4], Cristiano Longarini[4,23], Ryan A. Loomis[24], Frédéric Masset[25], Francois Menard[6], Ryuta Orihara[22], Daniel J. Price[7], Giovanni Rosotti[4], Jochen Stadler[6,26], Leonardo Testi[27,28], Hsi-Wei Yen[29], Gaylor Wafflard-Fernandez[6], David J. Wilner[8], Andrew J. Winter[3,14], Lisa Wölfer[1], Tomohiro C. Yoshida[10,30], and Brianna Zawadzki[31,32]

[1] Department of Earth, Atmospheric, and Planetary Sciences, Massachusetts Institute of Technology, Cambridge, MA 02139, USA
[2] Université Côte d'Azur, Observatoire de la Côte d'Azur, CNRS, Laboratoire Lagrange, France
[3] Max-Planck Institute for Astronomy (MPIA), Königstuhl 17, 69117 Heidelberg, Germany
[4] Dipartimento di Fisica, Università degli Studi di Milano, Via Celoria 16, 20133 Milano, Italy
[5] National Astronomical Observatory of Japan, Osawa 2-21-1, Mitaka, Tokyo 181-8588, Japan
[6] Univ. Grenoble Alpes, CNRS, IPAG, 38000 Grenoble, France
[7] School of Physics and Astronomy, Monash University, Clayton, VIC 3800, Australia
[8] Center for Astrophysics | Harvard & Smithsonian, Cambridge, MA 02138, USA
[9] Department of Astronomy, University of Florida, Gainesville, FL 32611, USA
[10] National Astronomical Observatory of Japan, 2-21-1 Osawa, Mitaka, Tokyo 181-8588, Japan
[11] Departamento de Astronomía, Universidad de Chile, Camino El Observatorio 1515, Las Condes, Santiago, Chile
[12] School of Physics & Astronomy, University of St. Andrews, North Haugh, St. Andrews, KY16 9SS, UK
[13] Centre for Exoplanet Science, University of St. Andrews, North Haugh, St. Andrews, KY16 9SS, UK
[14] Laboratoire Lagrange, Université Côte d'Azur, CNRS, Observatoire de la Côte d'Azur, 06304 Nice, France
[15] Department of Physics and Astronomy, The University of Georgia, Athens, GA 30602, USA
[16] Center for Simulational Physics, The University of Georgia, Athens, GA 30602, USA
[17] Institute for Artificial Intelligence, The University of Georgia, Athens, GA 30602, USA
[18] Department of Astronomy, Columbia University, 538 W. 120th Street, Pupin Hall, New York, NY, USA
[19] School of Physics and Astronomy, University of Leeds, Leeds LS2 9JT, UK
[20] Leiden Observatory, Leiden University, P.O. Box 9513, NL-2300 RA Leiden, The Netherlands
[21] European Southern Observatory, Karl-Schwarzschild-Str. 2, D-85748 Garching bei München, Germany
[22] College of Science, Ibaraki University, 2-1-1 Bunkyo, Mito, Ibaraki 310-8512, Japan
[23] Institute of Astronomy, University of Cambridge, Madingley Road, Cambridge CB3 0HA, UK
[24] National Radio Astronomy Observatory, 520 Edgemont Rd., Charlottesville, VA 22903, USA
[25] Instituto de Ciencias Físicas, Universidad Nacional Autónoma de México, Av. Universidad s/n, 62210 Cuernavaca, Mor., Mexico
[26] Université Côte d'Azur, Observatoire de la Côte d'Azur, CNRS, Laboratoire Lagrange, 06304 Nice, France
[27] Alma Mater Studiorum Università di Bologna, Dipartimento di Fisica e Astronomia (DIFA), Via Gobetti 93/2, 40129 Bologna, Italy
[28] INAF-Osservatorio Astrofisico di Arcetri, Largo E. Fermi 5, 50125 Firenze, Italy
[29] Academia Sinica Institute of Astronomy & Astrophysics, 11F of Astronomy-Mathematics Building, AS/NTU, No.1, Sec. 4, Roosevelt Rd, Taipei 10617, Taiwan
[30] Department of Astronomical Science, The Graduate University for Advanced Studies, SOKENDAI, 2-21-1 Osawa, Mitaka, Tokyo 181-8588, Japan
[31] Department of Astronomy, Van Vleck Observatory, Wesleyan University, 96 Foss Hill Drive, MiddleTown, CT 06459, USA
[32] Department of Astronomy & Astrophysics, 525 Davey Laboratory, The Pennsylvania State University, University Park, PA 16802, USA

Abstract

Planet formation is a hugely dynamic process requiring the transport, concentration, and assimilation of gas and dust to form the first planetesimals and cores. With access to observations with extremely high spatial and spectral resolution at unprecedented sensitivities, it is now possible to probe the planet-forming environment in detail. To this end, the exoALMA Large Program targeted 15 large protoplanetary disks, ranging between $\sim 1''$ and $\sim 7''$ in radius, and mapped the gas and dust distributions. ^{12}CO $J = 3–2$, ^{13}CO $J = 3–2$, and CS $J = 7–6$ molecular emission was imaged at high angular ($\sim 0''.15$) and spectral (~ 100 m s^{-1}) resolution, achieving a surface brightness temperature sensitivity of ~ 1.5 K over a single channel, while the 330 GHz continuum emission was imaged at 90 mas resolution and achieved a point source sensitivity of ~ 40 μJy beam^{-1}. These observations constitute some of the deepest observations of protoplanetary disks to date. Extensive substructure was found in all but one disk, traced by both dust continuum and molecular line emission. In addition, the molecular emission allowed for the velocity structure of the disks to be mapped with excellent precision (uncertainties of the order of 10 m s^{-1}), revealing a variety of kinematic perturbations across all sources. From this sample it is clear that, when observed in

---

[33] NASA Hubble Fellowship Program Sagan Fellow.

detail, all disks appear to exhibit physical and dynamical substructure indicative of ongoing dynamical processing due to young, embedded planets, large-scale (magneto)hydrodynamical instabilities or winds.

Unified Astronomy Thesaurus concepts: Protoplanetary disks (1300)

1. Introduction

It is now abundantly clear that the dust that settles into the planet-forming disk around a newly born star is highly structured, with numerous sources exhibiting gaps, rings, and spirals in their distributions (S. M. Andrews 2020; J. Bae et al. 2023). A similar substructuring in the chemical composition of the gas is observed, with varying morphologies found both between different molecules within a single source and from system to system (K. I. Öberg et al. 2023). This ubiquity of structure points toward a highly dynamic environment, one where the gas and dust distributions are continually sculpted by (magneto)hydrodynamical processes and/or a population of embedded protoplanets (J. Bae et al. 2023; G. Lesur et al. 2023).

Thus far the community has emphasized the ability of the Atacama Large Millimeter/submillimeter Array (ALMA) to image the distribution of millimeter-sized grains at spatial resolutions at the level of an astronomical unit (ALMA Partnership et al. 2015; S. M. Andrews et al. 2016; S. Pérez et al. 2019), and for its ability to catalog the chemical complexity across the planet formation process (S. Facchini et al. 2021; J. D. Ilee et al. 2021). In contrast, interest in observations optimized to study gas kinematics has only recently gained momentum, but has been rapidly growing ever since (C. Pinte et al. 2023). Early theoretical works have explored the use of gas kinematics to detect embedded planets (e.g., S. Perez et al. 2015); however, it was only through the claim of detection of a small sample of embedded protoplanets through their dynamical influence on the background disk that serious attention was paid to such observations (C. Pinte et al. 2018a, 2019; R. Teague et al. 2018a; P. Curone et al. 2024). These works demonstrated that gas dynamics was an alternative to searching for the millimeter-continuum emission from circumplanetary disks as a planet detection method (with PDS 70 being a notable exception; A. Isella et al. 2019; M. Benisty et al. 2021).

The realization that gas velocities could be constrained to a precision of less than $10\,\mathrm{m\,s^{-1}}$ (R. Teague et al. 2018a; S. Casassus & S. Pérez 2019; A. F. Izquierdo et al. 2022) and decomposed into azimuthally symmetric components (R. Teague et al. 2019a; H. Yu et al. 2021; A. F. Izquierdo et al. 2023) facilitated a range of analyses that proved particularly promising for characterizing the structure of the protoplanetary disk. Notable examples include the ability to detect super-Keplerian rotation attributed to the gravitational potential of moderately sized disks, leading to constraints on the disk mass (B. Veronesi et al. 2021; G. Lodato et al. 2023; P. Martire et al. 2024), deep searches for kinematic evidence of the gravitational instability (T. Paneque-Carreño et al. 2021; J. Speedie et al. 2024), and the identification of the launching of a disk wind (M. Galloway-Sprietsma et al. 2023).

In the context of this exoALMA Special Issue, the goal of this Letter is to set out the motivation, design, and implementation of the exoALMA Project, providing the background for the various studies that have been conducted using the data set, and it is organized as follows. We describe the scientific motivation for exoALMA in Section 2 and how this dictated the observational setup in Section 3. The resulting data products are discussed in Section 4, and Section 5 provides a brief summary of the main findings from the initial analysis of the data.

2. Scientific Motivation

There are a myriad of science goals that can be achieved with sensitive observations of high spatial and spectral resolution. While many overlap, or are strongly connected, those targeted by the exoALMA program can be broadly categorized into the following three subsections: planet hunting, Section 2.1; the dynamical structure of the protoplanetary disk, Section 2.2; and the physical structure of the protoplanetary disk, Section 2.3.

2.1. Embedded Protoplanets

The main motivation of the project is to detect the presence of embedded protoplanets. If detected, such objects provide a unique opportunity to better understand the planet formation process by demonstrating where planets are forming within a disk, place constraints on how quickly they form, and catalog from what material they are forming—all vital inputs to population synthesis models (e.g., C. Mordasini et al. 2012; D. H. Forgan et al. 2018). These snapshots of young planetary systems are crucial for confronting the vast populations of mature exoplanetary systems discovered thus far, providing insights as to the relative importance of varied initial conditions or different formation pathways in explaining the stunning diversity in exoplanetary demographics.

Although protoplanets are expected to be sufficiently luminous at near-infrared wavelengths to be readily detected with ground-based facilities, searches at these wavelengths have had limited success. While planetary sources such as PDS 70 b and c (M. Keppler et al. 2018; S. Y. Haffert et al. 2019) and HD 169142 b (I. Hammond et al. 2023) have been detected in multiple observations, the subtle signals of such embedded planets make identification and confirmation a hugely challenging prospect. One interpretation of this dearth of detections is that the sizable dust column from the circumstellar and circumplanetary disks results in significant levels of extinction that near-infrared photons simply cannot pierce (F. Alarcón & E. A. Bergin 2024; N. Choksi & E. Chiang 2025). Another, more provocative, explanation is that point-source-like features are not planets at all and instead could be explained by stellar light scattered from a structured protoplanetary disk (Y. Zhou et al. 2023), for example. Alternative detection methodologies are sorely needed.

To this end, several works have explored how such protoplanets may be detected in the submillimeter regime through their influence on their formation environment. These techniques have historically focused on localized enhancements in emission, either continuum emission, tracing a dust-rich circumplanetary disk (Z. Zhu et al. 2018), or molecular emission, attributed to the localized heating and desorption of volatiles in the immediate vicinity of the planet (L. I. Cleeves et al. 2015). As with the near-infrared searches, these approaches have had limited success, but two detections of continuum emission interpreted as circumplanetary disks have

been made in PDS 70 (A. Isella et al. 2019; M. Benisty et al. 2021), as well as a point source in line emission in AS 209 suggestive of a gas-rich circumplanetary disk (J. Bae et al. 2022). The small spatial scales of the emission and the challenges to achieve high dynamic range could be hampering such detections (S. M. Andrews et al. 2021).

A more promising avenue has been the study of how the planet may influence the structure of the gas in the protoplanetary disk and how these perturbations manifest in observations of molecular line emission (Disk Dynamics Collaboration et al. 2020). The most well studied of these interactions are the spiral shocks giving rise to spiral arms along Lindblad resonances in the midplane of the disk (R. R. Rafikov 2002), or buoyancy resonances in the atmosphere of the disk (J. Bae et al. 2021). While the density perturbations associated with such shocks are probably too subtle to be detected (J. Speedie & R. Dong 2022), the kinematic perturbations are expected to have velocities of up to $100 \, \mathrm{m \, s^{-1}}$, easily accessible with ALMA (F. Bollati et al. 2021; D. Fasano et al. 2024). Indeed, such perturbations have been identified and characterized in a large number of sources through localized features in the channel maps (typically described as "kinks" owing to the zigzag-like morphology; C. Pinte et al. 2018a, 2019, 2020, 2023) or in maps of the projected velocity after subtracting a background rotation model (R. Teague et al. 2019b, 2022; H. Garg et al. 2022), or using "folding" of the maps to subtract azimuthally symmetric structures (P. Huang et al. 2018b; A. F. Izquierdo et al. 2021, 2022, 2023; J. Stadler et al. 2023).

2.2. Dynamical Structure of Protoplanetary Disks

In addition to interactions with embedded planets, there are a number of other mechanisms that can drive velocity perturbations within a protoplanetary disk. Of particular note are the numerous (magneto)hydrodynamical instabilities that have been shown to be potentially active within a disk (G. Lesur et al. 2023). As these instabilities are the leading mechanism thought to facilitate the transport of angular momentum through turbulent viscosity, determining which of these instabilities dominate is a critical piece of the planet formation puzzle (C. F. Manara et al. 2023) because they govern the lifetime of the disk, setting the time available to form planets.

How each instability manifests in the data is dependent on the spatial scale of the velocity perturbations it drives and can be broadly split between what we term as "macro"-scale features, which we take as structures on the $\sim$10 au scale that are spatially resolved with typical observations, and "micro"-scale features, which are conversely spatially unresolved. For the former, numerical simulations have resulted in a variety of robust predictions. For example, the gravitational instability can drive large, multiple spiral arms (K. Kratter & G. Lodato 2016), which could be traced through dust overdensities (L. M. Pérez et al. 2016), localized heating of the gas (J. D. Ilee et al. 2011), or the velocity perturbations due to the shocks (C. Hall et al. 2020). Alternatively, the vertical shear instability, which has been modeled to result in large convection cells, appearing as concentric annular features in the gas velocity (M. Barraza-Alfaro et al. 2021), can drive the efficient vertical mixing of dust grains, resulting in large dust scale heights (M. Flock et al. 2020; C. P. Dullemond et al. 2022). As with any search for substructure, maximizing the angular resolution

of the observations will be critical in teasing out the subtle features.

On smaller scales, instabilities will manifest primarily as the broadening of molecular emission lines due to their contribution to the velocity dispersion along the line of sight (e.g., J. B. Simon et al. 2015). Searches for such broadening have aimed to use the radial and vertical variation in the level of nonthermal broadening to differentiate between different instabilities (A. M. Hughes et al. 2011; S. Guilloteau et al. 2012; K. M. Flaherty et al. 2015). For example, the magnetorotational instability should exhibit a strong dependence on height, with turbulent velocities increasing toward the disk atmosphere where the gas is more highly ionized (M. Flock et al. 2015), in contrast to the gravitational instability, where the strength of the velocity dispersions is independent of height above the midplane, but does depend on local scale height (D. Forgan et al. 2011). As the nonthermal velocity dispersion is expected to be small compared to the thermal velocity dispersion, data with high angular and spectral resolution where the emission lines are fully resolved are key in obtaining robust constraints on the level of broadening (R. Teague et al. 2016).

A complementary scenario to disk evolution being governed by instabilities is the idea of a (potentially magnetized) disk wind that is able to efficiently remove material from the disk (I. Pascucci et al. 2023). Detection and characterization of disk winds will allow for the refinement of analytical wind models routinely used to explain the global evolution of disks (B. Tabone et al. 2022; A. Somigliana et al. 2023). Regardless of the wind-launching mechanism, a disk wind is not expected to result in large velocity dispersions, but rather be dominated by large-scale flows, predominantly characterized by azimuthally symmetric radial components (A. Riols & G. Lesur 2018; T. J. Haworth & J. E. Owen 2020). As demonstrated by K. A. Rosenfeld et al. (2014), such radial velocities will manifest as a rotation of the projected velocity map, rather than the distinct features predicted by other instabilities. Here, both spatial and spectral resolution is necessary to decompose any wind component from the bulk Keplerian rotation of the protoplanetary disk.

2.3. Physical Structure of Protoplanetary Disks

To understand whether the conditions are suitable for the formation of planets or the growth of a particular instability, it is necessary to gain knowledge of the gas density and temperature structure of the disk.

In the high optical depth regime, typical of millimeter ^{12}CO, ^{13}CO line, and continuum emission, the brightness temperature acts as an accurate probe of the local gas temperature (E. Weaver et al. 2018). With ALMA observations now routinely resolving the vertical, as well as radial, structure of the disk, techniques like those presented by C. Pinte et al. (2018b) enable us to sample the two-dimensional temperature structure of disks that are only moderately inclined (C. J. Law et al. 2022). Such empirical measurements are critical for confronting the temperature structures that are used either as input for numerical simulations or to interpret observations. For example, although observations of hydrogen deuteride, HD, emission have been touted as a robust probe of the disk mass, the interpretation of the emission, and resulting disk mass, is highly dependent on the assumed temperature structure (M. K. McClure et al. 2016).

The limitation of this regime, however, is that the intensity of the line core is independent of the column density, and the considerably weaker line wings must be leveraged to learn about the column density. Instead, optically thin lines such as the rarer $C^{18}O$ and $C^{17}O$ isotopologues would offer an opportunity to more readily trace spatial variations in the local density; however, chemical processing will complicate the interpretation and limit application to the bulk gas disk (K. Zhang et al. 2017).

Fortuitously, the global disk density has been demonstrated to influence molecular line emission beyond its intensity, offering novel approaches to probing the disk density structure. One approach is to study the influence on the dynamics of the gas traced by the molecular emission. In addition to the gravitational potential from the host star, the radial pressure gradient and disk gravitational potential will modulate the rotation velocity of the gas, v_ϕ (K. A. Rosenfeld et al. 2013). Thus, with precise measurements of v_ϕ one can infer the background pressure profile (R. Teague et al. 2018a, 2018b) and, through comparison with the dust density profiles derived from continuum observations, explore the grain-trapping potential of pressure traps (G. P. Rosotti et al. 2020). Furthermore, with assumptions about the functional form of the background temperature and density structure, modeling of the v_ϕ profile can provide constraints on the disk mass with an accuracy of ~5% (S. M. Andrews et al. 2024; B. Veronesi et al. 2024, at least for systems where $M_{\mathrm{disk}}/M_* \gtrsim 0.05$). An alternative is to explore the influence on the profile of the line emission. For example, T. C. Yoshida et al. (2022) demonstrated that non-Gaussian line profiles are observed in regions of high density owing to the no-longer-negligible contribution of collisional broadening, providing tight constraints on the local volume density of the disk.

Clearly, improved constraints on such fundamental properties as the gas temperature and density profiles will be hugely important for the refinement of models and simulations, in terms of both making accurate predictions and interpreting future observations. For these goals, a combination of high spatial and spectral resolution is key. The spatial resolution is necessary to appropriately sample the spatial variation in emission and minimize unresolved intensity gradients, while spectral resolution is critical for detecting the subtle variations in line profile.

3. Observational Design

Motivated by this range of science goals, it was clear that obtaining deep, spatially and spectrally resolved observations of a large sample of protoplanetary disks would offer a powerful opportunity to make significant progress in several areas. In this section, we discuss how the observations were designed to maximize the scientific potential of the data set.

3.1. Sources

When developing the source list for the exoALMA program, several aspects needed to be balanced: sources must represent new frontiers (i.e., minimize reobserving common targets), be well suited for the scientific goals, and be readily observable throughout the cycle. The first condition essentially precluded any source that had already been observed extensively in long-baseline configurations with ALMA, such as the five sources from the MAPS Large Program (AS 209, HD 163296, GM

Aur, IM Lup, and MWC 480; K. I. Öberg et al. 2021), TW Hya (R. Teague et al. 2019b, 2022), HD 169142 (H. Yu et al. 2021; H. Garg et al. 2022), HD 97048 (C. Pinte et al. 2019), and HD 100546 (A. S. Booth et al. 2024).

In terms of scientific applicability, four aspects were considered: brightness, radial extent, obscuration, and inclination. A bright disk is necessary to image the data at a high velocity sampling (brighter sources would provide higher signal-to-noise ratios (SNRs) with narrower channel spacing), while a large disk is necessary to maximize the number of independent spatial samples across it that can be measured. Verifying that there is no absorption or contamination from large-scale emission, such as a remnant envelope, would ensure that all channels would be usable in the analysis. Even if a source is large, bright, and unobscured, if it is viewed at an unfavorably high inclination then many typically employed analyses would fail. Most notably, at high inclinations, $i \gtrsim 60°$, the near and far emission lobes characteristic of a rotating source become confused with emission arising from the top and bottom surfaces of the disk (see the discussion for the highly inclined Gomez's Hamburger shown by R. Teague et al. 2020, for example). While such highly inclined sources offer an opportunity to study the vertical structure of the disk (particularly when considering just the dust continuum; M. Villenave et al. 2020), the need to assume a dynamical model to "deproject" the molecular line data precludes any kinematical studies (A. Dutrey et al. 2017; D. Ruíz-Rodríguez et al. 2021).

The final criterion was the distribution of sources in R.A. to aid in scheduling observations. As Band 7 observations require typically better weather conditions than the more commonly used (at least for protoplanetary disks) Band 6, a wide spread in R.A. was selected to ensure that there was a high chance for the complete sample to be observed in a single cycle. In practice, this required limiting the number of sources from any given star-forming region. A discussion of why Band 7 was chosen over Band 6 can be found in the following subsection.

These considerations led to three conditions for source selection. The sources must all have a gas extent of at least $1''$ in radius, have an inclination that falls between 5° and 60°, and show no evidence of envelope emission in archival data. The total intensity of the archival ^{12}CO emission was not used as an absolute criterion, but rather to decide between sources that otherwise appeared equally suitable given the scheduling constraints.

The resulting 15 sources targeted with exoALMA are described in Table 1. It is important to note that these considerations resulted in a decidedly biased sample of disks in terms of whether they represent the broader protoplanetary disk population. As demonstrated by the stellar properties listed in Table 1, these disks tend to be around more massive and luminous stars and have a larger fraction of transition disks or azimuthal asymmetries in their dust continuum. Indeed, all but PDS 66 exhibit gaplike or cavity-like structures in their continuum emission (which does show a ring in near-infrared scattered light; S. G. Wolff et al. 2016), as discussed by P. Curone et al. (2025). While this may limit the applicability of findings to smaller, potentially more "typical" protoplanetary disks, this sample represents the best opportunity to demonstrate ALMA's ability to map gas kinematics in a protoplanetary disk, yielding the data necessary to develop the techniques necessary to extend these studies to a larger, more representative sample.

Table 1
exoALMA Sample

Source	Alias	R.A.	Decl.	SpT	d (pc)	RUWE[a]	References
DM Tau	⋯	04 33 48.733	+18 10 09.973	M1	144	1.49	1
AA Tau	⋯	04 34 55.420	+24 28 53.034	M0	135	3.33	2
LkCa 15	⋯	04 39 17.791	+22 21 03.390	K5	157	1.36	1
HD 34282	⋯	05 16 00.477	−09 48 35.394	A0.5	309	1.41	3
MWC 758	⋯	05 30 27.529	+25 19 57.076	A3	156	0.99	4
CQ Tau	⋯	05 35 58.467	+24 44 54.091	F2	149	3.70	4
SY Cha	⋯	10 56 30.388	−77 11 39.402	K5	182	1.37	5
PDS 66	MP Mus	13 22 07.542	−69 38 12.219	K1	98	0.96	6
HD 135344B	SAO 206462	15 15 48.446	−37 09 16.024	F4	135	0.91	7
HD 143006	⋯	15 58 36.913	−22 57 15.221	G7	167	1.13	8
RXJ1604.3-2130 A	J1604	16 04 21.642	−21 30 29.058	K2	145	1.75	8
RXJ1615.3-3255	J1615	16 15 20.234	−32 55 05.098	K5	156	1.55	9
V4046 Sgr	⋯	18 14 10.482	−32 47 34.517	K5	72	0.86	10
RXJ1842.9-3532	J1842	18 42 57.981	−35 32 42.827	K2	151	1.10	11
RXJ1852.3-3700	J1852	18 52 17.301	−37 00 11.949	K2	147	1.58	12

Note. References for spectral types (SpT): 1, S. J. Kenyon & L. Hartmann (1995); 2, G. H. Herbig (1977); 3, V. Piétu et al. (2003); 4, V. Mannings & A. I. Sargent (2000); 5, A. Frasca et al. (2015); 6, O. Schütz et al. (2005); 7, C. A. Grady et al. (2009); 8, K. L. Luhman & E. E. Mamajek (2012); 9, R. Wichmann et al. (1999); 10, S. V. Nefs et al. (2012); 11, J. M. Carpenter et al. (2005); 12 C. F. Manara et al. (2014).
[a] Renormalized unit weight error from Gaia (Gaia Collaboration et al. 2023).

3.2. Telescope Setup

In order to achieve the aforementioned goals we opted for a relatively simple spectral setup, consisting of four spectral windows, three of which were assigned to a single molecular line, ^{12}CO $J = 3$–2, ^{13}CO $J = 3$–2, and CS $J = 7$–6, and one for continuum emission centered at 332 GHz (0.9 mm). Optically thick CO isotopologues provide the best opportunity to trace the gas structure due to their abundance, while their large optical depth results in their observed emission arising from only a narrow layer in the disk, justifying the use of the simple "two-layer" morphological models often used for interpreting the data (e.g., R. Teague et al. 2018a; S. Casassus & S. Pérez 2019; A. F. Izquierdo et al. 2021). With its relatively large abundance among the simple species accessible simultaneously with CO such that high-SNR observations were likely to be achieved for many sources, CS was the third molecule chosen, providing access to a region close to the disk midplane (A. Dutrey et al. 2017). Interestingly for kinematical studies, its large molecular weight, $\mu = 44$, limits its sensitivity to thermal broadening compared to the lighter CO isotopologues ($\mu \approx 28$), making it ideal for searches for turbulence through nonthermal broadening (S. Guilloteau et al. 2012; R. Teague et al. 2016, 2018c).

The three line spectral windows were configured to use the maximum spectral sampling of 15 kHz, resulting in a spectral resolution of 30.5 kHz (27 m s^{-1}) when accounting for the signal processing associated with the correlator. The continuum window was centered at 332 GHz (0.9 mm) and set to frequency division mode, yielding a spectral resolution of 488.281 kHz (440 m s^{-1}) across a bandwidth of 1875 MHz. The choice to observe transitions that fall in Band 7 rather than the more commonly targeted Band 6 transitions was driven primarily by the desire to maximize the velocity resolution of the data: a frequency resolution of 30.5 kHz corresponds to a velocity resolution of 27 m s^{-1} at 345 GHz, but only 40 m s^{-1} at 230 GHz. This higher velocity resolution allows the FWHM of an emission line to be sampled ∼10 times, allowing for a precise characterization of the line profile while also remaining sensitive to subtle deviations in the line profiles arising to due

spatially unresolved structures (D. D. Lenz & T. R. Ayres 1992). Although rarely used, obtaining the data at such a fine velocity resolution provides confidence that any spectral features observed are real, rather than due to sampling or averaging effects that arise for lower spectral resolutions. Furthermore, to achieve a typical rms sensitivity of 1.5 K, Band 7 requires a factor of ∼3 times shorter integrations than Band 6, allowing for a substantially larger sample to be considered.

As discussed in Section 2, obtaining a high spatial resolution is key if features in the gas are to be accurately associated with the features observed in (typically higher spatial resolution) dust continuum observations. Guided by the images of CO isotopologue emission released by the MAPS Large Program (K. I. Öberg et al. 2021), a target spatial resolution of 0″.1 (14 au at 140 pc) was chosen as a trade-off between imaging quality and the general scales of features observed in the dust continuum (e.g., J. Huang et al. 2018a). It was found that a combination of configurations C43-3 and C43-6 would result in the desired angular resolution. A handful of sources (DM Tau, LkCa 15, HD 34282, J1604, J1615, V4046 Sgr, and AA Tau) were known to have molecular emission extending close to, if not beyond, the maximum recoverable scale of 4″.7 and were therefore additionally observed with the Atacama Compact Array, extending the maximum recoverable scale to 19″.3.

3.3. Observations

Data were collected between 2021 October and 2023 May and delivered to the collaboration after an initial quality assurance check and pipeline calibration by ALMA. R. Loomis et al. (2025) describe the subsequent calibration and imaging procedures conducted by the exoALMA team upon delivery of the data.

4. The exoALMA Data Set

4.1. Overview

The exoALMA Data Set comprises observations of 15 sources with emission from ^{12}CO $J = 3$–2, ^{13}CO $J = 3$–2, CS $J = 7$–6, and 332 GHz continuum. In addition to strong
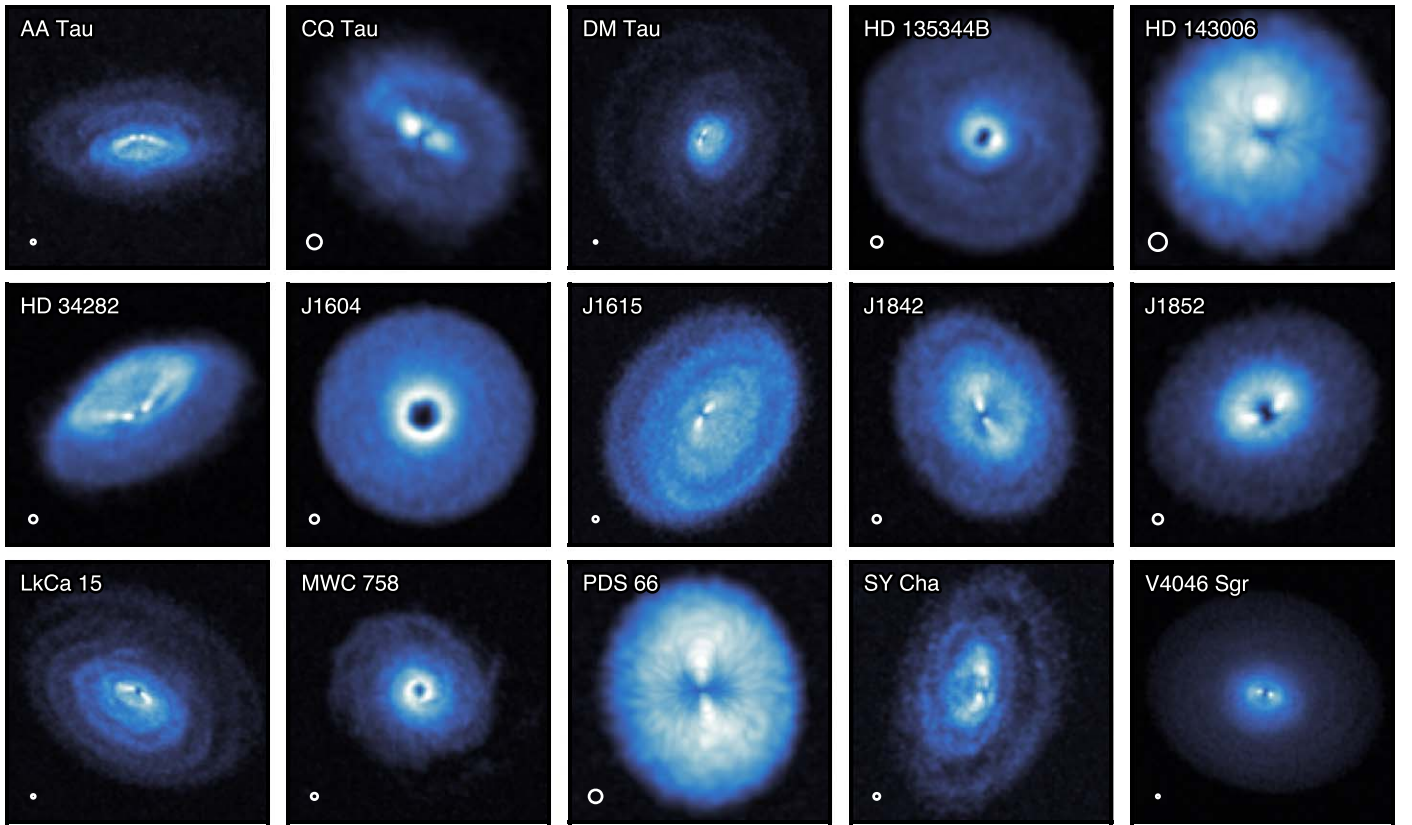
Figure 1. A summary of the exoALMA sample with all sources showing evidence of gas substructures. All images show the ^{12}CO (3–2) peak intensity obtained with `bettermoments` (R. Teague & D. Foreman-Mackey 2018) using a quadratic fit to the data and masked with the CLEAN masks. Each source has a variable field of view, and the open circle in the lower left of each image denotes the 0″15 synthesized beam for reference. The color maps are individually scaled for each source to emphasize the emission morphology rather than for a quantitative comparison (which is provided by M. Galloway-Sprietsma et al. 2025).

detections of the continuum emission, all molecules were robustly detected in every source and no cloud contamination was found for any of the lines.

Figure 1 presents an overview of the continuum-subtracted ^{12}CO peak intensity of the exoALMA sample using the "fiducial" imaging set, described below, highlighting the diversity in morphologies and structures observed. It is clear from this figure alone that these disks have gas that is highly structured, which is perhaps unsurprising given the apparent ubiquity of structure observed in the dust continuum (S. M. Andrews 2020; P. Curone et al. 2025). Similar galleries for the ^{13}CO and CS emission can be found in the Appendix.

4.2. Data Products

To accurately quantify and characterize the level and complexity of gaseous substructures hosted by these disks, a range of data products were produced and analyzed as part of the collaboration using a range of techniques described by A. F. Izquierdo et al. (2025). Prior to the application of these techniques, all pieces of software used were benchmarked to ensure that (a) all predictions and retrievals are accurate and (b) there is consistency among the tools adopted within the exoALMA collaboration (J. Bae et al. 2025).

4.2.1. Image Sets

A number of different image sets for the line and continuum emission were produced to satisfy the range of different criteria required by the various projects: a "fiducial" set, a "high

resolution" set, and a "low resolution" set. The "fiducial" set was designed to be appropriate for the broadest range of scientific questions with moderate angular and spectral resolutions, the "high resolution" sets focused on maximizing angular resolution while sacrificing spectral sampling or sensitivity, and the "low resolution" enhanced the surface brightness sensitivity of the images. A comparison of channel maps from each of these sets is shown in Figure 2 for the case of LkCa 15, and the implementation and results of the imaging process discussed by R. Loomis et al. (2025) and summarized in their Tables 3, 4, and 5.

Fiducial Images. The fiducial images used a variable robust value with a source-specific uv-taper to obtain a circular 0″15 synthesized beam and were imaged with a channel spacing of $100 \, \text{m s}^{-1}$ for ^{12}CO and ^{13}CO, and $200 \, \text{m s}^{-1}$ for CS. The circularized beam, rather than the elliptical beam that is obtained by default, was deemed to introduce less confusion in the interpretation of features in image-plane analyses. The $100 \, \text{m s}^{-1}$ velocity spacing was found to provide a good trade-off between spectrally resolving the line and maintaining a strong signal in a single channel for imaging. The considerably weaker emission of CS compared to the CO isotopologues required a coarser velocity sampling of $200 \, \text{m s}^{-1}$ to conserve the per-channel imaging quality. Figure 3 shows an example of the "fiducial" image set for HD 135344B, displaying maps of the peak intensity of the molecular emission, along with a continuum emission. For the case of the continuum images, a default robust value of -0.5 was chosen, which resulted in a typical beam size of $\sim 90 \, \text{mas}$. No tapering was applied,
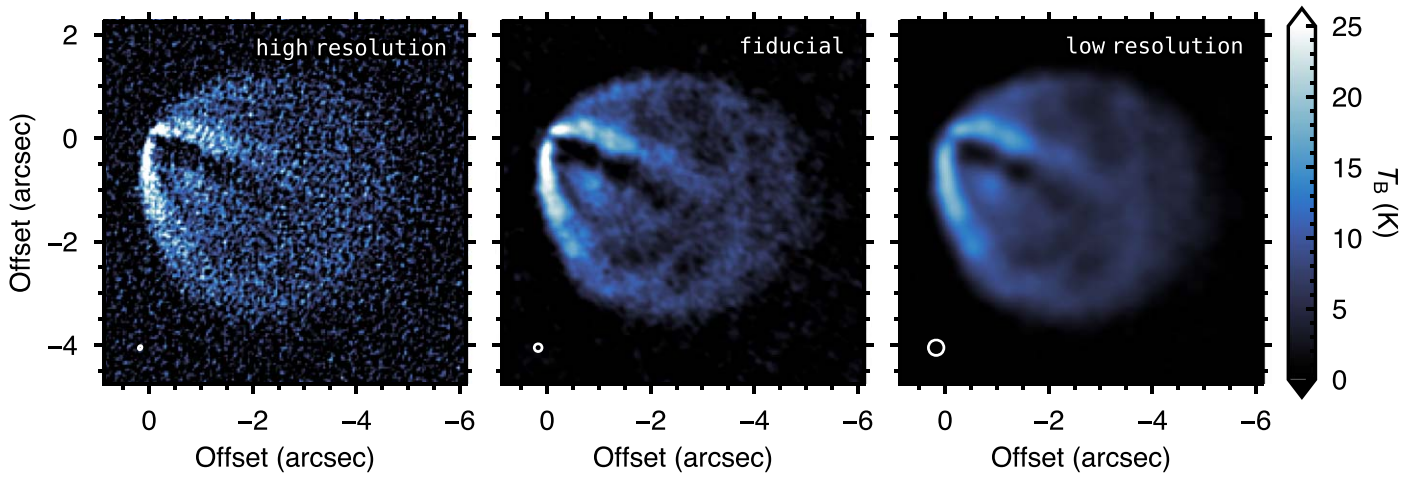
Figure 2. ^{12}CO emission, converted to brightness temperature using the Rayleigh–Jeans approximation, from the disk around LkCa 15, demonstrating the differences between the three different imaging sets released with the exoALMA program: "high" resolution, left; "fiducial," center; and "low," right. The spatial resolution and channel spacing for each image are, from left to right, 86 mas × 67 mas and 200 m s^{-1}, 0.″15 × 0.″15 and 100 m s^{-1}, and 0.″3 × 0.″3 and 100 m s^{-1}. Note that the "high" resolution image sets have variable angular resolutions set by the requirement of resolving the continuum substructure.
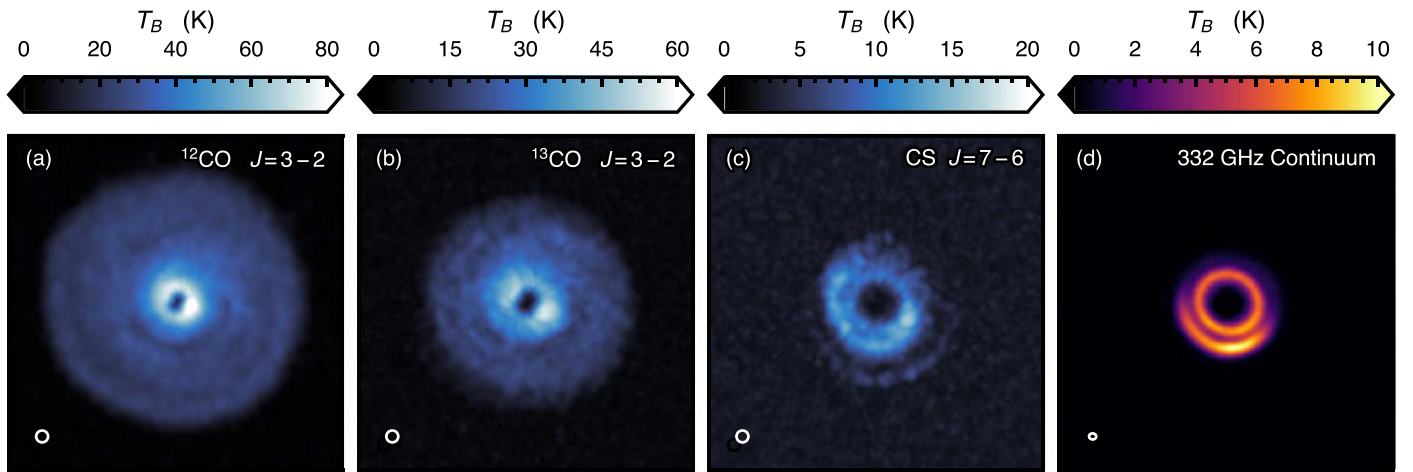
Figure 3. Example of the peak intensities derived from the "fiducial set" of images for HD 135344B. All panels share a 4″ × 4″ field of view centered on the star. The spatial resolution of molecular emission images is 0.″15 and the channel spacing is 100 m s^{-1} for both ^{12}CO and ^{13}CO and 200 m s^{-1} for CS. The continuum image has a synthesized beam of 90 mas × 76 mas with a position angle of 85.°0.

resulting in a noncircular beam, unlike the line data. An example of a fiducial continuum image is shown in Figure 3(d). A thorough discussion of the continuum imaging process is provided by P. Curone et al. (2025).

High Resolution Images. A major goal of the exoALMA program is to compare the structure found in the gas with the dust distribution (e.g., J. Stadler et al. 2025; C. T. Yoshida et al. 2025). However, the 0.″15 resolution of the fiducial images, ∼20 au at 140 pc, is insufficient to resolve variations across the observed dust substructures (P. Curone et al. 2025). This motivated the "high resolution" imaging set, where each source was imaged with a robust value that yields a synthesized beam that is ∼0.5 times smaller than the average size of a dust substructure for that source, resulting in beams from 65 mas for HD 34282 up to the fiducial 150 mas. For these images, the channel spacing was reduced for most sources as it was found that a coarser sampling of 200 m s^{-1} was necessary to maintain a robust detection of the emission to accurately trace the large velocity gradients found in the inner regions of the disk, except for AA Tau and J1604, where the 100 m s^{-1} channel spacing could be maintained. At these higher angular resolutions, the sensitivities dropped by a factor of

∼5 relative to the "fiducial set," with typical rms brightness temperatures of 7.5 K. Table 4 of R. Loomis et al. (2025) details the angular resolution and channel spacing adopted for each source along with the resulting noise level.

Images with High Surface Brightness Sensitivity. A similar limitation was faced in the outer regions of the disk with the fiducial images: weaker, more extended emission was less well reconstructed, resulting in a poor determination of the properties of the edge of the disk. This prompted the generation of "low resolution" images, which were identical to the fiducial images except for a circularized 0.″3 synthesized beam. While losing information on smaller spatial scales compared to the other two image sets, this set provided a considerably better representation of the large-scale emission distribution, particularly for the larger, more diffuse disks such as DM Tau and LkCa 15, where determination of the emission surface was a challenge (M. Galloway-Sprietsma et al. 2025). These images typically had rms brightness temperatures around 0.25 K in 100 m s^{-1} channels.

Regularized Maximum Likelihood Imaging. In addition to the standard CLEAN-based imaging, B. Zawadzki et al. (2025) explores the use of regularized maximum likelihood
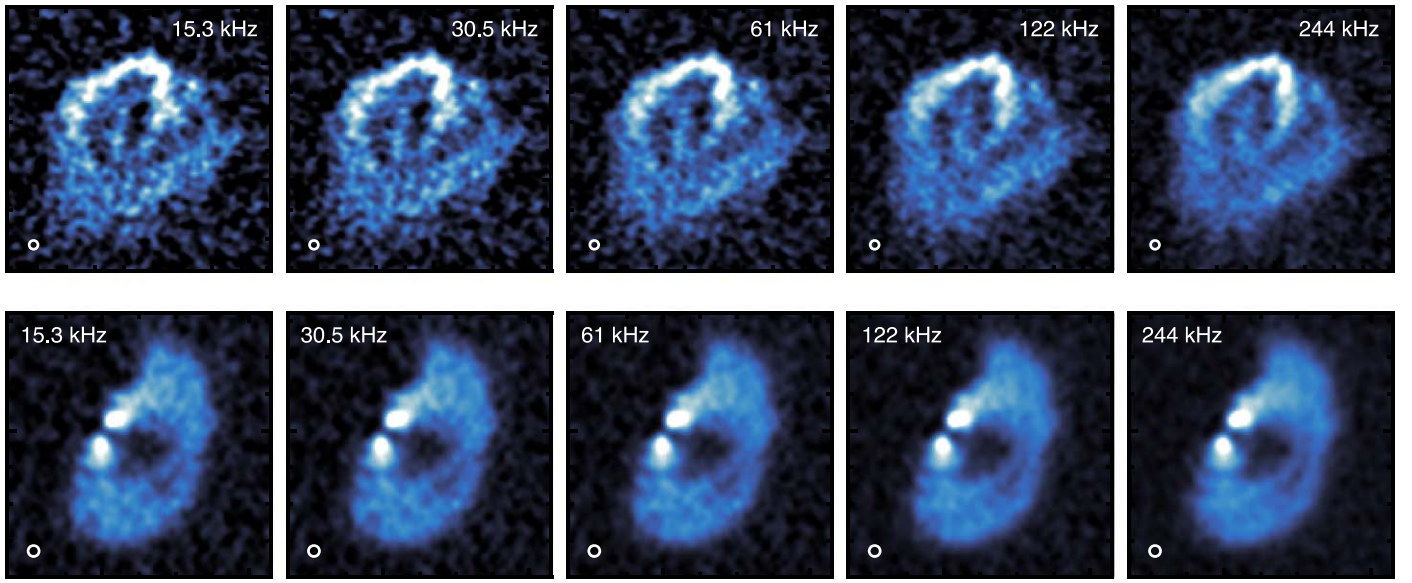
Figure 4. Channel maps of ^{12}CO emission from SY Cha (top) and HD 135344B (bottom), showing the effect of different channel widths. The channel widths, labeled at the top of each panel, correspond to 13.3, 26.4, 52.9, 105.8, and 211.5 m s^{-1} at the rest frequency of ^{12}CO. Each channel was CLEANed down to 3× the rms measured in a line-free region of the image. Note that while the background noise is reduced with coarser channel widths, structures in the emission morphology can be washed out. Also note that the finest channel sampling of 15.3 kHz, the native channel spacing, is actually below the spectral resolution of the data so would suffer from considerable covariance with adjacent channels (R. A. Loomis et al. 2018).

(RML) imaging, which uses a different set of assumptions when creating the image compared to CLEAN. Specifically, in RML imaging, the model is the image itself and the user provides information about how the pixel values can vary spatially and in relation to nearby pixels. Conversely, CLEAN builds an image through the summation of multiple Gaussian components. This difference in image reconstruction was used as a test of the robustness of the features found in the images of the molecular emission for several sources (AA Tau, HD 135344B, J1604, J1615, J1842, LkCa 15, and SY Cha; C. Pinte et al. 2025) and of the sensitivity of emission surface and gas temperature extraction for sources with large, diffuse emission.

Channel Spacing. As shown in Figure 4, the data could be imaged with narrower or broader channel spacing as long as this is no finer than the spectral resolution of the data (30.5 kHz ≈ 27 m s^{-1}). However, the quality of the non-Keplerian features is impacted, depending on what channel spacing is chosen. With broad channel spacing, kinematic features are poorly resolved spectrally (they are essentially smoothed out in the channel) and thus are hard to identify in the images. For narrow channel spacing, the features are spectrally well-resolved, but there is insufficient signal in a single channel for a robust image reconstruction, often leading to confusion as to what is a real feature. In the "fiducial" imaging sets generated for exoALMA, the finest channel spacing adopted was 100 m s^{-1} for ^{12}CO and ^{13}CO emission, and 200 m s^{-1} for CS emission, as these were found to provide a good balance between excellent imaging quality and spectrally resolving the features of interest. The raw data and calibrated measurement sets from the project, however, support the imaging of data at a finer channel spacing if one so desires.

4.2.2. General System Properties

For all sources, general system properties were derived following analyses of the continuum and line emission described in detail by P. Curone et al. (2025), and by A. F. Izquierdo et al. (2025) and M. Galloway-Sprietsma et al. (2025), respectively, and provided in Table 2. These include the orientation of the disk on the sky, parameterized by the inclination, i, and position angle, PA, measured from north to the redshifted major axis in a counterclockwise direction. These were used in conjunction with Gaia-derived distances for the sources (Gaia Collaboration et al. 2016, 2023), summarized in Table 1, to derive a dynamical stellar mass of the host star using the discminer modeling approach described by A. F. Izquierdo et al. (2025). This kinematically derived stellar mass is the stellar mass that best describes the observed rotation of the gas assuming a purely Keplerian profile and neglecting the effects of vertical stratification, radial pressure gradients, or self-gravity, which are discussed by J. Stadler et al. (2025) and C. Longarini et al. (2025). Table 2 also includes a summary of the sorts of substructures detected in the continuum, with P. Curone et al. (2025) providing more details.

Integrated intensities of each of the three emission lines and the integrated flux density of the continuum emission for each source were also calculated. For the calculation of the fluxes, the continuum-subtracted "fiducial" image set was used along with a circular aperture with a radius of $1.2 \times r_{\rm out}$ where $r_{\rm out}$ was taken from M. Galloway-Sprietsma et al. (2025). The flux density of the continuum also used the "fiducial" continuum images and integrated the emission within a source-specific mask. The reader is referred to P. Curone et al. (2025) for more details. For all four measurements, the ~10% uncertainties associated with flux calibration are significantly larger than the statistical uncertainties due to noise in the data.

4.2.3. Moment Maps

The line emission for each source was summarized in different moment maps: an integrated intensity map ("zeroth moment" map), a peak intensity map, a line center map, and a line width map. As discussed by R. Teague & D. Foreman-Mackey (2018), there are multiple approaches to deriving the line center (and analogously, the line width), which involve different assumptions

Table 2
exoALMA Derived Source Properties

Source	M_* ($M_\odot$)	i [a] (deg)	PA [b] (deg)	$F_{^{12}CO}$ (Jy km s^{-1})	$F_{^{13}CO}$ (Jy km s^{-1})	F_{CS} (Jy km s^{-1})	F_{cont} (mJy)	Continuum Substructure [c]
DM Tau	0.45	38.7	335.7	33.37 ± 0.50	8.99 ± 0.31	0.70 ± 0.06	226.5 ± 0.6	R, A, I
AA Tau	0.79	−58.7	272.7	22.77 ± 0.38	4.82 ± 0.21	1.82 ± 0.17	189.4 ± 0.3	R, I, W
LkCa 15	1.14	50.3	62.1	33.83 ± 0.40	9.83 ± 0.39	1.59 ± 0.12	407.1 ± 0.4	R, C
HD 34282	1.61	−58.3	117.4	17.82 ± 0.06	6.03 ± 0.06	0.66 ± 0.03	343.4 ± 0.3	R, A
MWC 758	1.40	19.4	240.3	21.02 ± 0.23	5.46 ± 0.19	0.50 ± 0.20	214.5 ± 0.2	R, A, I
CQ Tau	1.40	−36.3	235.1	9.89 ± 0.11	3.33 ± 0.13	0.64 ± 0.05	431.9 ± 0.3	R, S, C
SY Cha	0.77	−52.4	346.2	17.39 ± 0.32	3.57 ± 0.27	0.85 ± 0.08	158.4 ± 0.5	R, A, I
PDS 66	1.28	−31.9	189.0	11.00 ± 0.10	2.72 ± 0.10	1.07 ± 0.07	336.1 ± 0.2	
HD 135344B	1.61	−16.1	242.9	18.00 ± 0.13	6.19 ± 0.14	0.52 ± 0.07	424.7 ± 0.2	R, A, C
HD 143006	1.56	−16.9	168.9	6.42 ± 0.08	1.84 ± 0.08	0.40 ± 0.04	155.5 ± 0.2	R, A, I, W
RXJ1604.3-2130 A	1.29	6.0	258.1	18.29 ± 0.45	7.01 ± 0.55	1.26 ± 0.18	198.4 ± 0.3	R, C
RXJ1615.3-3255	1.14	46.5	325.4	30.51 ± 0.30	10.28 ± 0.22	0.96 ± 0.12	386.0 ± 0.7	R, I
V4046 Sgr	1.73 [d]	−34.1	255.7	59.89 ± 0.42	17.05 ± 0.24	3.01 ± 0.11	668.4 ± 1.0	R, I
RXJ1842.9-3532	1.07	39.4	205.9	14.75 ± 0.16	3.11 ± 0.13	0.61 ± 0.05	141.5 ± 0.2	R, C
RXJ1852.3-3700	1.03	−32.7	117.1	10.83 ± 0.13	3.69 ± 0.11	1.66 ± 0.05	150.9 ± 0.1	R, C

Notes. M_*, i, and PA are derived from `discminer` analyses of the ^{12}CO emission and are described by A. F. Izquierdo et al. (2025). Typical `discminer` uncertainties are around 0.1% for these parameters; however T. Hilder et al. (2025) suggest spatial correlations can increase these by a factor of ~10. The fluxes, $F_{^{12}CO}$, $F_{^{13}CO}$, and F_{CS}, were calculated by integrating zeroth moment maps in a circular aperture with a radius of $1.2 \times r_{out}$ where r_{out} was taken from M. Galloway-Sprietsma et al. (2025). F_{cont} is calculated from the fiducial continuum images, as described by P. Curone et al. (2025).
[a] As discussed by A. F. Izquierdo et al. (2025), the negative sign is used to assign whether the northern edge of the disk is tilted toward or away from us. For comparisons with continuum data, taking the absolute value is appropriate.
[b] Defined as the angle between north and the redshifted major axis of the disk in a counterclockwise direction.
[c] Types of substructure include rings, R; azimuthal asymmetries, A; spirals, S; inner disk, I; cavity, C; and warps, W, based on P. Curone et al. (2025).
[d] Combined dynamical mass of the spectroscopic binary.

about the intrinsic line profile and orientation of the disk on the sky. A. F. Izquierdo et al. (2025) discuss the various approaches taken by the exoALMA collaboration, including a decomposition of the emission arising from the front and back sides of the disk (e.g., I. de Gregorio-Monsalvo et al. 2013; K. A. Rosenfeld et al. 2013), to calculate these maps.

4.2.4. Vertical and Radial Emission Structure

The moment maps described above can be further collapsed into one-dimensional radial profiles through an azimuthal average. P. Curone et al. (2025) and M. Galloway-Sprietsma et al. (2025) discuss the application to the continuum and the molecular line peak intensity, respectively, and catalog the features, such as gaps and rings, found in the radial profiles, following the procedure described by J. Huang et al. (2018a) and C. J. Law et al. (2021a). Notably, most sources were found to exhibit structure in their radial emission profiles aside from PDS 66, consistent with previous findings (Á. Ribas et al. 2023).

For sources with an inclination greater than 20°—the a majority of the sample—the emission heights of the three molecular lines were determined using the method presented by C. Pinte et al. (2018b) as implemented in `disksurf` (R. Teague et al. 2021) and described in detail by M. Galloway-Sprietsma et al. (2025), and using `discminer` (A. F. Izquierdo et al. 2021) and described by A. F. Izquierdo et al. (2025). These two approaches are complementary because `disksurf` recovers a nonparametric emission surface after adopting general source parameters, while `discminer` fits a parameterized disk model to the data, including a smooth emission surface, while allowing the general source parameters to freely vary. A more thorough comparison of these methods is given by M. Galloway-Sprietsma et al. (2025). The three molecules trace distinct vertical regions within the disk and provide probes of the physical and dynamical conditions at those

heights, enabling studies of the vertical dependence of physical processes within the disk. As with the substructure identification in the radial intensity profiles, M. Galloway-Sprietsma et al. (2025) characterize variations in the emission surface and discuss (anti) correlations with the substructures found in the dust continuum.

4.2.5. Temperature Structures

Assuming that the ^{12}CO and ^{13}CO emission is optically thick, the brightness temperature as a function of radius and height can be used to derive empirical two-dimensional temperature structures for all the sources (e.g., C. J. Law et al. 2021b). M. Galloway-Sprietsma et al. (2025) use these profiles, derived from the "fiducial" images, to fit standard parametric forms for the two-dimensional temperature structure (E. Dartois et al. 2003) to each of the sources.

4.2.6. Velocity Profiles

With constraints on the height above the midplane that the molecular emission arises from in hand, the emission morphology could be correctly deprojected and rotation profiles derived for each molecular line and each source (correctly accounting for the projection effects of a vertically extended disk is crucial in deriving accurate rotation curves; e.g., S. M. Andrews et al. 2024). J. Stadler et al. (2025) describe the process of extracting the rotation profiles and identify subtle radial variations that can be attributed to underlying variations in pressure gradient (R. Teague et al. 2018a, 2018b; G. P. Rosotti et al. 2020). A disk-wide analysis of the profiles is described by C. Longarini et al. (2025), which allows for robust determinations of a dynamical disk mass for 10 sources (e.g., B. Veronesi et al. 2021; G. Lodato et al. 2023). Dynamical disk masses could not be measured for sources where strong azimuthal asymmetries in the disk emission prevented reliable v_ϕ
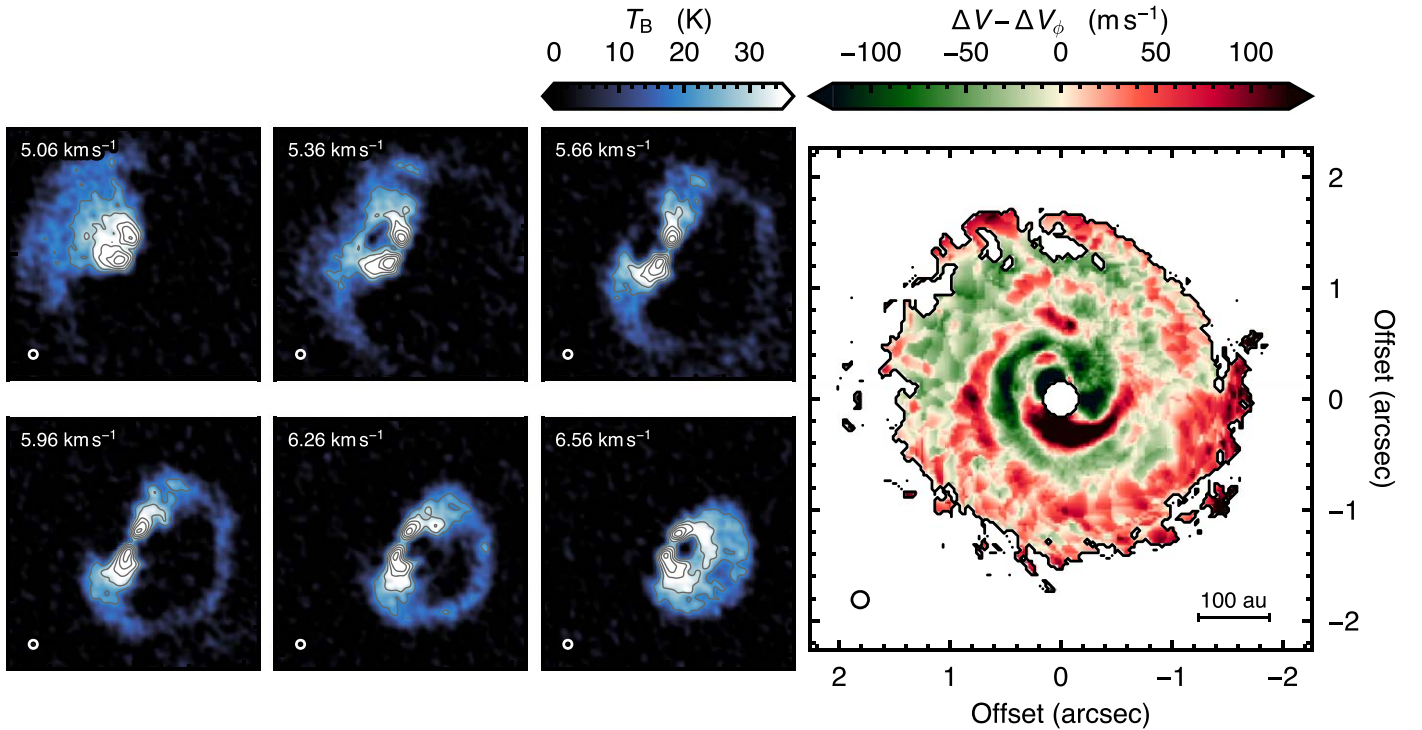
Figure 5. The high sensitivity of the exoALMA data reveals structures and subtle perturbations previously undetectable. As an example, the channel maps show ^{12}CO emission from the disk around MWC 758, which exhibits significant non-Keplerian components, such as the large arc in the southwest of the disk. C. Pinte et al. (2025) leverage this sensitivity to look for indications of embedded planets in the exoALMA sources. Similarly, the right panel shows the variations in line width of the ^{12}CO emission after subtracting an azimuthally averaged value, revealing a striking spiral morphology. A. F. Izquierdo et al. (2025) describe how such analyses were conducted for the exoALMA sample and how they were characterized. All panels share the same field of view and the 0″15 beam is shown in the lower left corner of each.

measurements (MWC 758 and CQ Tau) or sources viewed at low inclinations such that the vertical emission height of the molecule could not be determined (HD 135344B, HD 143006, and RXJ1604.3-2130 A; C. Longarini et al. 2025).

As is clear from Figure 1, all sources exhibit some level of azimuthal structure, which will bias the recovered rotation profiles because the extraction methods assume that any azimuthal variation is due to azimuth-dependent projection effects rather than intrinsic azimuthal variations (C. Pinte et al. 2023). However, as discussed by A. F. Izquierdo et al. (2025), testing has demonstrated that these biases are small in all but the most extreme of cases and can thus be used with confidence to study the global structure of the protoplanetary disk.

A calculation and analysis of the azimuthally averaged radial profiles of the radial and vertical velocities will be discussed in a forthcoming series of papers.

4.3. Data Access

All of the data products will be publicly available both through the ALMA archive as products associated with project ID `2021.1.01123.L` and through the exoALMA website.[34]

5. Summary of exoALMA Results

The exoALMA Project surveyed 15 protoplanetary disks and obtained observations with high spatial ($\sim 0''15$) and spectral (~ 100 m s^{-1}) resolution of ^{12}CO $J = 3$–2, ^{13}CO $J = 3$–2, CS $J = 7$–6, and 332 GHz continuum emission, enabling a comprehensive mapping of the physical and dynamical

structure of the planet-forming environment. These observations definitively show that protoplanetary disks harbor extensive substructure in their gas distributions, evident in the density, temperature, and kinematics of the disk.

This observing program has provided a unique look at the planet-forming environment—one that has challenged the conventional understanding of disk structure, dynamics, and contemporary analysis techniques. The complexity of these observations catalyzed a comprehensive assessment of the commonly adopted imaging techniques (R. Loomis et al. 2025; B. Zawadzki et al. 2025), numerical methods (J. Bae et al. 2025), and analysis methodologies (T. Hilder et al. 2025; A. F. Izquierdo et al. 2025) to ensure information was robustly and reproducibly extracted from the data. An initial, and by no means exhaustive, analysis of the data using these techniques, described in the Letters published alongside this one, demonstrates the huge potential of this data set. A summary of the main findings from the first wave of exoALMA Letters is discussed below, while results more broadly related to the 2D velocity structure will be the focus of future publications.

1. High-resolution observations revealed that protoplanetary disks exhibit extensive substructure in molecular line emission. Consistent with previous studies of protoplanetary disks, all exoALMA sources exhibit substructure in their dust continuum (P. Curone et al. 2025). While predominantly annular in nature, several sources host localized clumps and azimuthal asymmetries. Strikingly, all sources also displayed extensive structure in their molecular emission morphology, most readily seen in the ^{12}CO emission, but also in the ^{13}CO and CS emission for several brighter sources (A. F. Izquierdo et al. 2025; C. Pinte et al. 2025; B. Zawadzki et al. 2025), as presented in Figure 5. Variations in

---
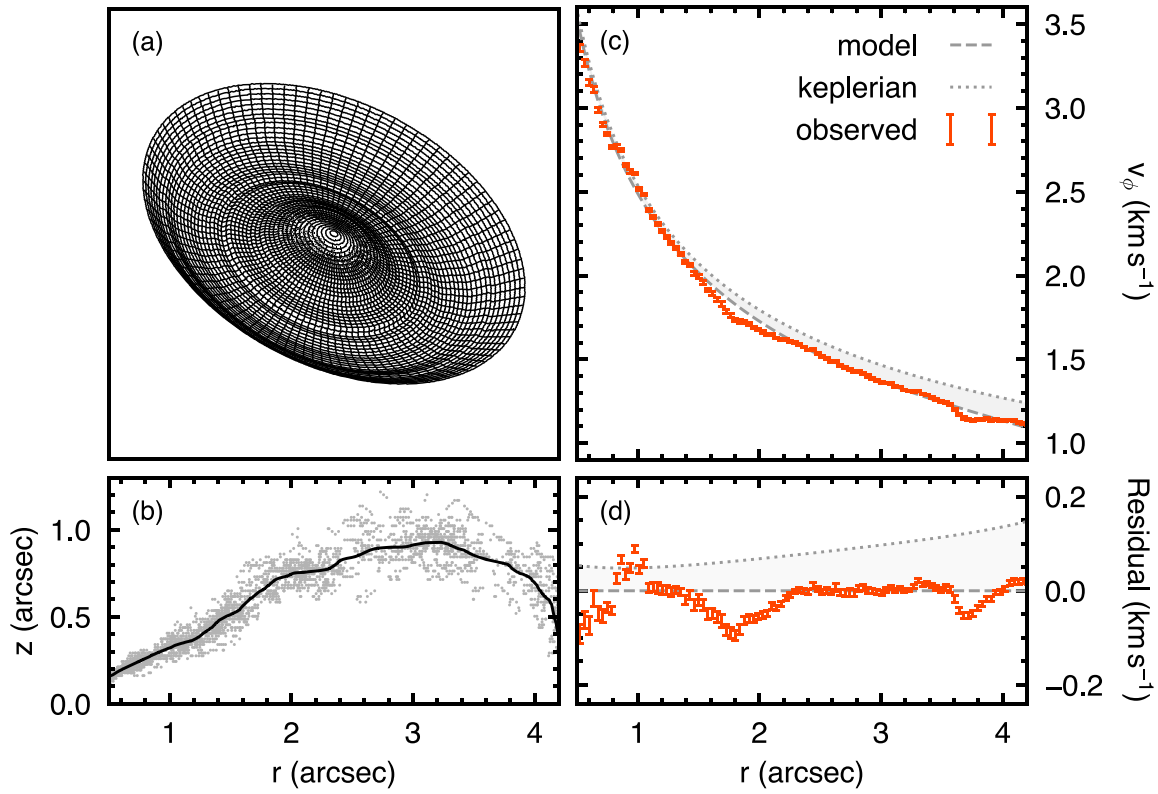
Figure 6. The high angular and spectral resolution of the exoALMA data enables a detailed exploration of the 3D physical and dynamical structure of protoplanetary disks. Panel (a) shows the projection of the inferred emission surface of the ^{12}CO emission from the disk around LkCa 15 shown in panel (b). As described by M. Galloway-Sprietsma et al. (2025), the gray points are individual measurements while the black line shows a moving average with a window of 0″15. This deprojection allows for a precise v_ϕ profile to be extracted, as shown by the orange points in panel (c), which reveals a significant departure from purely Keplerian rotation, as shown by the dotted gray line (J. Stadler et al. 2025). The global profile can be well recovered with a model, shown by the gray line, that includes a radial pressure gradient and the inclusion of the self-gravity of the disk (C. Longarini et al. 2025). The localized variations, most readily discernible in the residuals shown in panel (d), can be associated with localized pressure variations within the disk (J. Stadler et al. 2025).

the optically thick ^{12}CO emission may be attributed to localized changes in gas temperature, surface density, or non-Keplerian motion (M. Galloway-Sprietsma et al. 2025; J. Stadler et al. 2025), while similar variations found in the line wings, or in the optically thinner ^{13}CO and CS emission, pointed toward variations in gas density (C. T. Yoshida et al. 2025). Observations of the quality obtained by the exoALMA project unambiguously demonstrate the ubiquity of localized structure outside ∼15 au, the bulk of the disk for these sources, ideal for revealing the processes that sculpt the disk such as planet–disk interactions, (magneto)hydrodynamical instabilities, or stellar fly-bys.

2. Characterization of the vertical structure of moderately inclined protoplanetary disks yielded novel insights to the physical structure of those disks. M. Galloway-Sprietsma et al. (2025) and A. F. Izquierdo et al. (2025) measured the emitting surfaces for all molecules for each source with a favorable inclination, finding the vertical chemical stratification expected for the ^{12}CO, ^{13}CO, and CS emission. The spatially resolved vertical structure, as demonstrated in Figure 6, enabled the derivation of empirical 2D temperature distributions (M. Galloway-Sprietsma et al. 2025), as well as constraints on the CO column density and gas surface density profiles (G. Rosotti et al. 2025). Critically, the improved angular resolution and sensitivity revealed many structures in the emission surfaces previously undetected, which indicate substantial variations in the density structure of disks. Furthermore, with a large sample of emission surfaces to hand, a linear relationship between the

average emission height, z/r, and the disk mass was observed (M. Galloway-Sprietsma et al. 2025).

3. The extraction of extremely precise rotation curves that achieve a precision of down to ∼10 m s^{-1} revealed kinematic perturbations, up to 15% relative to the background rotation, indicative of variations in gas surface density correlated with dust substructures. Figures 6(c) and (d) demonstrate the quality of the v_ϕ profiles that could be derived for LkCa 15 using the exoALMA data. Interpreting these variations as pressure variations, J. Stadler et al. (2025) demonstrated that pressure maxima and minima are coincident with the spatially resolved continuum rings and gaps, highly suggestive of grain trapping. These findings are strengthened by the detection of the pressure broadening of ^{12}CO emission at the location of a bright continuum ring in the disk of RXJ1604.3-2130 A, suggesting a dust trapping scenario (C. T. Yoshida et al. 2025). For most cases where the dust structures can be spatially resolved by these data, the recovered velocity profiles convincingly show that the grains are dynamically trapped in pressure maxima.

4. Mapping the influence of the gravitational potential of the protoplanetary disk on the rotation profiles facilitates powerful constraints on the gas surface density and enables a calibration of chemistry-based mass measurements. C. Longarini et al. (2025) were able to self-consistently model the gas rotational velocity profiles for 10 sources to place tight constraints on the disk mass and gas surface density profile, finding that all sources should be stable against the gravitational instability. Figures 6(c) and (d) compare a purely
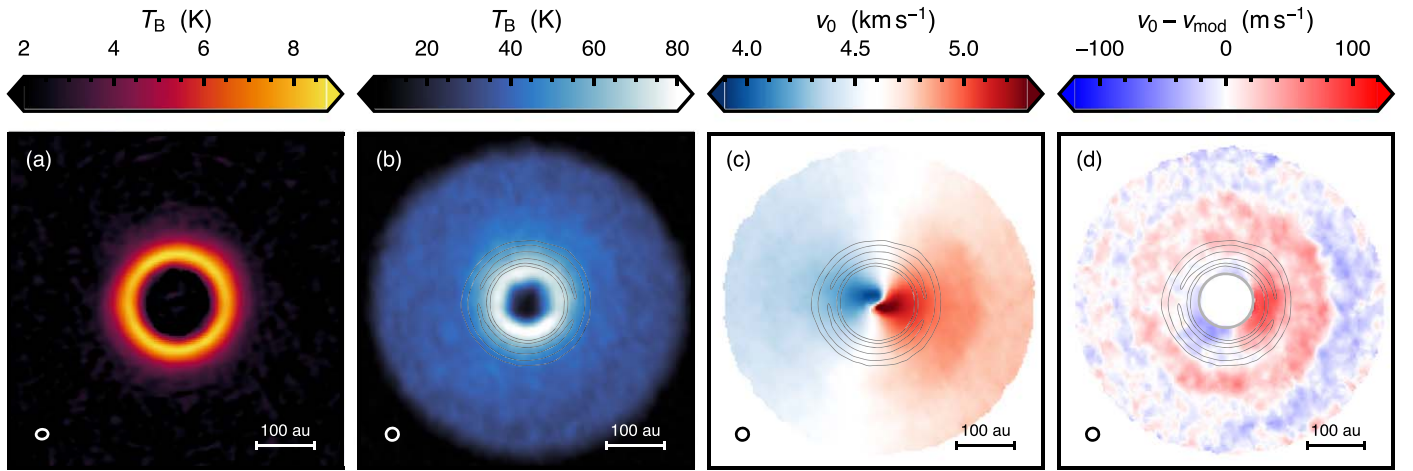
Figure 7. Combined analyses of the gas structure and dynamics with the dust substructure can provide insights into the physical processes sculpting the disk. These four panels display emission from the disk around RXJ1604.3-2130 A with (a) showing the dust continuum reported by P. Curone et al. (2025), (b) the ^{12}CO peak intensity, and (c) the inferred projected velocity, v_0, with A. F. Izquierdo et al. (2025) describing the techniques used to calculate these. Panel (d) shows the residual velocity structure after subtracting a purely Keplerian model, revealing substantial deviations that can be associated with pressure variations (J. Stadler et al. 2025; C. T. Yoshida et al. 2025).

Keplerian model with a dotted line, and the best fit model for LkCa 15 from C. Longarini et al. (2025) as a dashed gray line, clearly demonstrating a significant departure from Keplerian rotation due to the self-gravity of the disk and the radial pressure gradient. In parallel, L. Trapman et al. (2025) used complementary observations of N_2H^+ to calibrate commonly used chemistry-based approaches to disk mass measurement, finding broad agreement—a factor of $\sim$3—between the two methods.

5. A combined analysis of dust and gas substructures allows for direct comparisons with numerical simulations to identify the processes that are driving the observed features. Figure 7 provides an example of such a comparison for RXJ1604.3-2130 A, contrasting the continuum and ^{12}CO emission morphology with the derived gas velocity structure. M. Barraza-Alfaro et al. (2025) explored the ability of exoALMA quality observations to differentiate between different (magneto)hydrodynamical instabilities based on the morphology of the temperature, density, and kinematic perturbations they drive. C. Gardner et al. (2025) conducted an in depth exploration of the LkCa 15 disk and the possibility of embedded planets driving the structures observed, and L. Wölfer et al. (2025) scrutinized the dynamics associated with azimuthal structures in the continuum believed to be vortices. C. Pinte et al. (2025) discussed these localized perturbations in the context of possible embedded planets.

These works demonstrate that investing in observations that push the spatial and spectral resolution of ALMA while achieving the sensitivity necessary to map out molecular line emission will facilitate significant leaps in our understanding of the planet formation environment. Although the generalization of these findings to the global population of protoplanetary disks may be hampered by the sample selection, this program has unambiguously demonstrated the utility of deep, long-baseline observations of protoplanetary disks in probing the physical conditions of planet formation. The extensive data release will hopefully seed many new projects that generate new insights into how the planet formation process proceeds.

Appendix
Peak Intensity Maps

In this Appendix we present the peak intensity maps of the ^{13}CO $J = 3$–2 and CS $J = 7$–6 emission for all the exoALMA sources in Figures 8 and 9, respectively. As with Figure 1, the "fiducial set" of images were used, meaning a spatial resolution of $0\rlap{.}''15$ for all lines and a channel spacing of $100\,\mathrm{m\,s^{-1}}$ for ^{12}CO and ^{13}CO and a coarser $200\,\mathrm{m\,s^{-1}}$ for the CS. The azimuthal asymmetries observed in the CS emission are due to radiative transfer effects arising from low-optical-depth emission that is in a ring morphology, which results in a larger projected column density around the major axis of the disk. bettermoments was used for the peak extraction using a quadratic fit to the line profile. For a gallery of the continuum emission we refer the reader to P. Curone et al. (2025).
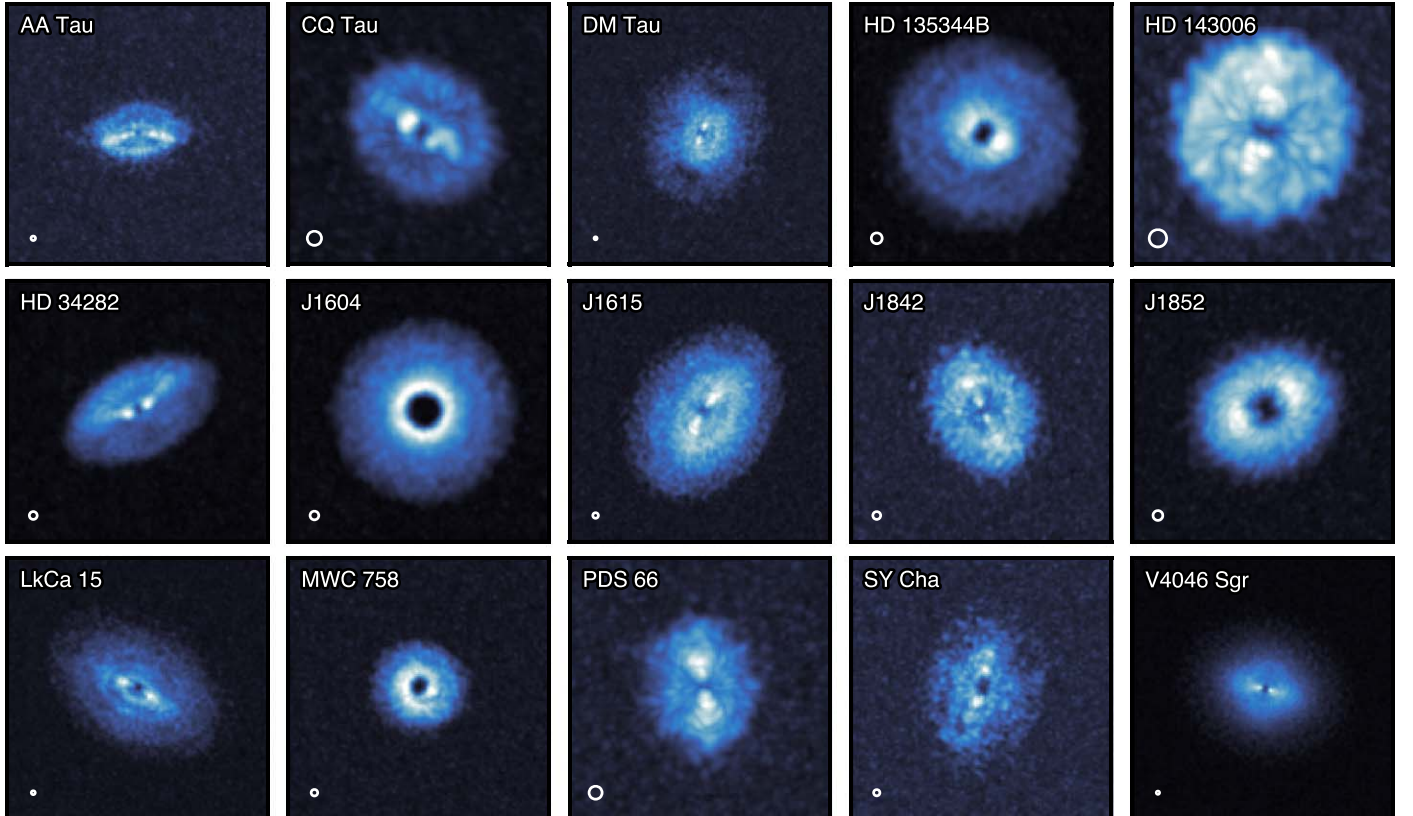
Figure 8. Gallery of ^{13}CO $J = 3$–2 emission from the exoALMA sources. The field of view of each panel is the same as that in Figure 1. The $0\rlap{.}''15$ beam is shown in the lower left corner. The linear color scaling is set to span up to 95% of the peak value in each panel.
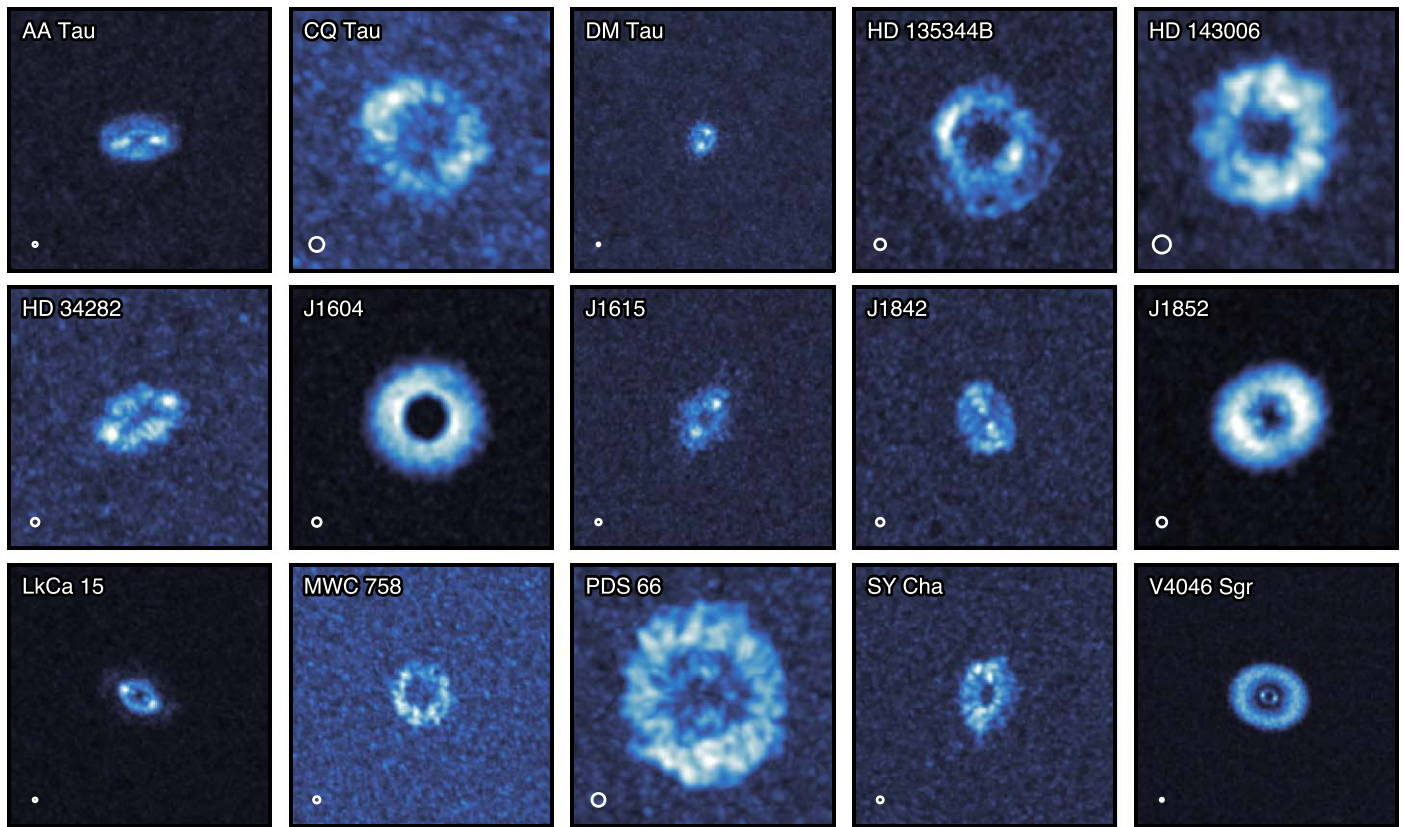
Figure 9. Peak intensity of the CS $J = 7–6$ emission for all exoALMA sources. The field of view of each panel is the same as that in Figure 1. The 0″15 beam is shown in the lower left corner. The linear color scaling is set to span up to 95% of the peak value in each panel.

ORCID iDs

Richard Teague ⬤ https://orcid.org/0000-0003-1534-5186
Myriam Benisty ⬤ https://orcid.org/0000-0002-7695-7605
Stefano Facchini ⬤ https://orcid.org/0000-0003-4689-2684
Misato Fukagawa ⬤ https://orcid.org/0000-0003-1117-9213
Christophe Pinte ⬤ https://orcid.org/0000-0001-5907-5179
Sean M. Andrews ⬤ https://orcid.org/0000-0003-2253-2270
Jaehan Bae ⬤ https://orcid.org/0000-0001-7258-770X
Marcelo Barraza-Alfaro ⬤ https://orcid.org/0000-0001-6378-7873
Gianni Cataldi ⬤ https://orcid.org/0000-0002-2700-9676
Nicolás Cuello ⬤ https://orcid.org/0000-0003-3713-8073
Pietro Curone ⬤ https://orcid.org/0000-0003-2045-2154
Ian Czekala ⬤ https://orcid.org/0000-0002-1483-8811
Daniele Fasano ⬤ https://orcid.org/0000-0003-4679-4072
Mario Flock ⬤ https://orcid.org/0000-0002-9298-3029
Maria Galloway-Sprietsma ⬤ https://orcid.org/0000-0002-5503-5476
Himanshi Garg ⬤ https://orcid.org/0000-0002-5910-4598
Cassandra Hall ⬤ https://orcid.org/0000-0002-8138-0425
Iain Hammond ⬤ https://orcid.org/0000-0003-1502-4315
Thomas Hilder ⬤ https://orcid.org/0000-0001-7641-5235
Jane Huang ⬤ https://orcid.org/0000-0001-6947-6072
John D. Ilee ⬤ https://orcid.org/0000-0003-1008-1142
Andrés F. Izquierdo ⬤ https://orcid.org/0000-0001-8446-3026
Kazuhiro Kanagawa ⬤ https://orcid.org/0000-0001-7235-2417
Geoffroy Lesur ⬤ https://orcid.org/0000-0002-8896-9435
Giuseppe Lodato ⬤ https://orcid.org/0000-0002-2357-7692
Cristiano Longarini ⬤ https://orcid.org/0000-0003-4663-0318
Ryan A. Loomis ⬤ https://orcid.org/0000-0002-8932-1219

Frédéric Masset ⬤ https://orcid.org/0000-0002-9626-2210
Francois Menard ⬤ https://orcid.org/0000-0002-1637-7393
Ryuta Orihara ⬤ https://orcid.org/0000-0003-4039-8933
Daniel J. Price ⬤ https://orcid.org/0000-0002-4716-4235
Giovanni Rosotti ⬤ https://orcid.org/0000-0003-4853-5736
Jochen Stadler ⬤ https://orcid.org/0000-0002-0491-143X
Leonardo Testi ⬤ https://orcid.org/0000-0003-1859-3070
Hsi-Wei Yen ⬤ https://orcid.org/0000-0003-1412-893X
Gaylor Wafflard-Fernandez ⬤ https://orcid.org/0000-0002-3468-9577
David J. Wilner ⬤ https://orcid.org/0000-0003-1526-7587
Andrew J. Winter ⬤ https://orcid.org/0000-0002-7501-9801
Lisa Wölfer ⬤ https://orcid.org/0000-0002-7212-2416
Tomohiro C. Yoshida ⬤ https://orcid.org/0000-0001-8002-8473
Brianna Zawadzki ⬤ https://orcid.org/0000-0001-9319-1296

References

Alarcón, F., & Bergin, E. A. 2024, ApJ, 967, 144
ALMA Partnership, Brogan, C. L., Pérez, L. M., et al. 2015, ApJL, 808, L3
Andrews, S. M. 2020, ARA&A, 58, 483
Andrews, S. M., Teague, R., Wirth, C. P., Huang, J., & Zhu, Z. 2024, ApJ, 970, 153
Andrews, S. M., Elder, W., Zhang, S., et al. 2021, ApJ, 916, 51
Andrews, S. M., Wilner, D. J., Zhu, Z., et al. 2016, ApJL, 820, L40
Bae, J., Flock, M., Izquierdo, A., et al. 2025, ApJL, 984, L12
Bae, J., Isella, A., Zhu, Z., et al. 2023, in ASP Conf. Ser. 534, Protostars and Planets VII, ed. S. Inutsuka et al. (San Francisco, CA: ASP)
Bae, J., Teague, R., Andrews, S. M., et al. 2022, ApJL, 934, L20
Bae, J., Teague, R., & Zhu, Z. 2021, ApJ, 912, 56
Barraza-Alfaro, M., Flock, M., Béthune, W., et al. 2025, ApJL, 984, L21
Barraza-Alfaro, M., Flock, M., Marino, S., & Pérez, S. 2021, A&A, 653, A113
Benisty, M., Bae, J., Facchini, S., et al. 2021, ApJL, 916, L2
Bollati, F., Lodato, G., Price, D. J., & Pinte, C. 2021, MNRAS, 504, 5444

Booth, A. S., Leemker, M., van Dishoeck, E. F., et al. 2024, AJ, 167, 164
Carpenter, J. M., Wolf, S., Schreyer, K., Launhardt, R., & Henning, T. 2005, AJ, 129, 1049
Casassus, S., & Pérez, S. 2019, ApJL, 883, L41
Choksi, N., & Chiang, E. 2025, MNRAS, 537, 2945
Cleeves, L. I., Bergin, E. A., & Harries, T. J. 2015, ApJ, 807, 2
Curone, P., Facchini, S., Andrews, S. M., et al. 2025, ApJL, 984, L9
Curone, P., Izquierdo, A. F., Testi, L., et al. 2022, A&A, 665, A25
Dartois, E., Dutrey, A., & Guilloteau, S. 2003, A&A, 399, 773
de Gregorio-Monsalvo, I., Ménard, F., Dent, W., et al. 2013, A&A, 557, A133
Disk Dynamics Collaboration, Armitage, P. J., & Bae, J. 2020, arXiv:2009.04345
Dullemond, C. P., Ziampras, A., Ostertag, D., & Dominik, C. 2022, A&A, 668, A105
Dutrey, A., Guilloteau, S., Piétu, V., et al. 2017, A&A, 607, A130
Facchini, S., Teague, R., Bae, J., et al. 2021, AJ, 162, 99
Fasano, D., Winter, A. J., Benisty, M., et al. 2024, A&A, 687, A223
Flaherty, K. M., Hughes, A. M., Rosenfeld, K. A., et al. 2015, ApJ, 813, 99
Flock, M., Ruge, J. P., Dzyurkevich, N., et al. 2015, A&A, 574, A68
Flock, M., Turner, N. J., Nelson, R. P., et al. 2020, ApJ, 897, 155
Forgan, D., Rice, K., Cossins, P., & Lodato, G. 2011, MNRAS, 410, 994
Forgan, D. H., Hall, C., Meru, F., & Rice, W. K. M. 2018, MNRAS, 474, 5036
Frasca, A., Biazzo, K., Lanzafame, A. C., et al. 2015, A&A, 575, A4
Gaia Collaboration, Prusti, T., de Bruijne, J. H. J., et al. 2016, A&A, 595, A1
Gaia Collaboration, Vallenari, A., Brown, A. G. A., et al. 2023, A&A, 674, A1
Galloway-Sprietsma, M., Bae, J., Izquierdo, A., et al. 2025, ApJL, 984, L10
Galloway-Sprietsma, M., Bae, J., Teague, R., et al. 2023, ApJ, 950, 147
Gardner, C., Isella, A., Other, A., et al. 2025, ApJL, 984, L16
Garg, H., Pinte, C., Hammond, I., et al. 2022, MNRAS, 517, 5942
Grady, C. A., Schneider, G., Sitko, M. L., et al. 2009, ApJ, 699, 1822
Guilloteau, S., Dutrey, A., Wakelam, V., et al. 2012, A&A, 548, A70
Haffert, S. Y., Bohn, A. J., de Boer, J., et al. 2019, NatAs, 3, 749
Hall, C., Dong, R., Teague, R., et al. 2020, ApJ, 904, 148
Hammond, I., Christiaens, V., Price, D. J., et al. 2023, MNRAS, 522, L51
Haworth, T. J., & Owen, J. E. 2020, MNRAS, 492, 5030
Herbig, G. H. 1977, ApJ, 214, 747
Hilder, T., Casey, A. R., Price, D. J., et al. 2025, ApJL, 984, L13
Huang, J., Andrews, S. M., Dullemond, C. P., et al. 2018a, ApJL, 869, L42
Huang, P., Isella, A., Li, H., Li, S., & Ji, J. 2018b, ApJ, 867, 3
Hughes, A. M., Wilner, D. J., Andrews, S. M., Qi, C., & Hogerheijde, M. R. 2011, ApJ, 727, 85
Ilee, J. D., Boley, A. C., Caselli, P., et al. 2011, MNRAS, 417, 2950
Ilee, J. D., Walsh, C., Booth, A. S., et al. 2021, ApJS, 257, 9
Isella, A., Benisty, M., Teague, R., et al. 2019, ApJL, 879, L25
Izquierdo, A. F., Facchini, S., Rosotti, G. P., van Dishoeck, E. F., & Testi, L. 2022, ApJ, 928, 2
Izquierdo, A. F., Stadler, J., Bae, J., et al. 2025, ApJL, 984, L8
Izquierdo, A. F., Testi, L., Facchini, S., Rosotti, G. P., & van Dishoeck, E. F. 2021, A&A, 650, A179
Izquierdo, A. F., Testi, L., Facchini, S., et al. 2023, A&A, 674, A113
Kenyon, S. J., & Hartmann, L. 1995, ApJS, 101, 117
Keppler, M., Benisty, M., Müller, A., et al. 2018, A&A, 617, A44
Kratter, K., & Lodato, G. 2016, ARA&A, 54, 271
Law, C. J., Crystian, S., Teague, R., et al. 2022, ApJ, 932, 114
Law, C. J., Loomis, R. A., Teague, R., et al. 2021a, ApJS, 257, 3
Law, C. J., Teague, R., Loomis, R. A., et al. 2021b, ApJS, 257, 4
Lenz, D. D., & Ayres, T. R. 1992, PASP, 104, 1104
Lesur, G., Flock, M., Ercolano, B., et al. 2023, in ASP Conf. Ser. 534, Protostars and Planets VII, ed. S. Inutsuka et al. (San Francisco, CA: ASP), 465
Lodato, G., Rampinelli, L., Viscardi, E., et al. 2023, MNRAS, 518, 4481
Longarini, C., Lodato, G., Rosotti, G., et al. 2025, ApJL, 984, L17
Loomis, R., Facchini, S., Benisty, M., et al. 2025, ApJL, 984, L7
Loomis, R. A., Öberg, K. I., Andrews, S. M., et al. 2018, AJ, 155, 182
Luhman, K. L., & Mamajek, E. E. 2012, ApJ, 758, 31
Manara, C. F., Ansdell, M., Rosotti, G. P., et al. 2023, in ASP Conf. Ser. 534, Protostars and Planets VII, ed. S. Inutsuka et al. (San Francisco, CA: ASP)
Manara, C. F., Testi, L., Natta, A., et al. 2014, A&A, 568, A18
Mannings, V., & Sargent, A. I. 2000, ApJ, 529, 391
Martire, P., Longarini, C., Lodato, G., et al. 2024, A&A, 686, A9

McClure, M. K., Bergin, E. A., Cleeves, L. I., et al. 2016, ApJ, 831, 167
Mordasini, C., Alibert, Y., Klahr, H., & Henning, T. 2012, A&A, 547, A111
Nefs, S. V., Birkby, J. L., Snellen, I. A. G., et al. 2012, MNRAS, 425, 950
Öberg, K. I., Facchini, S., & Anderson, D. E. 2023, ARA&A, 61, 287
Öberg, K. I., Guzmán, V. V., Walsh, C., et al. 2021, ApJS, 257, 1
Paneque-Carreño, T., Pérez, L. M., Benisty, M., et al. 2021, ApJ, 914, 88
Pascucci, I., Cabrit, S., Edwards, S., et al. 2023, in ASP Conf. Ser. 534, Protostars and Planets VII, ed. S. Inutsuka et al. (San Francisco, CA: ASP)
Pérez, L. M., Carpenter, J. M., Andrews, S. M., et al. 2016, Sci, 353, 1519
Pérez, S., Casassus, S., Baruteau, C., et al. 2019, AJ, 158, 15
Perez, S., Dunhill, A., Casassus, S., et al. 2015, ApJL, 811, L5
Piétu, V., Dutrey, A., & Kahane, C. 2003, A&A, 398, 565
Pinte, C., Ilee, J. L., Huang, J., et al. 2025, ApJL, 984, L15
Pinte, C., Ménard, F., Duchêne, G., et al. 2018b, A&A, 609, A47
Pinte, C., Price, D. J., Ménard, F., et al. 2018a, ApJL, 860, L13
Pinte, C., Price, D. J., Ménard, F., et al. 2020, ApJL, 890, L9
Pinte, C., Teague, R., Flaherty, K., et al. 2023, in ASP Conf. Ser. 534, Protostars and Planets VII, ed. S. Inutsuka et al. (San Francisco, CA: ASP)
Pinte, C., van der Plas, G., Ménard, F., et al. 2019, NatAs, 3, 1109
Rafikov, R. R. 2002, ApJ, 569, 997
Ribas, Á., Macías, E., Weber, P., et al. 2023, A&A, 673, A77
Riols, A., & Lesur, G. 2018, A&A, 617, A117
Rosenfeld, K. A., Andrews, S. M., Hughes, A. M., Wilner, D. J., & Qi, C. 2013, ApJ, 774, 16
Rosenfeld, K. A., Chiang, E., & Andrews, S. M. 2014, ApJ, 782, 62
Rosotti, G., Longarini, C., Paneque-Carreño, T., et al. 2025, ApJL, 984, L20
Rosotti, G. P., Teague, R., Dullemond, C., Booth, R. A., & Clarke, C. J. 2020, MNRAS, 495, 173
Ruíz-Rodríguez, D., Kastner, J., Hily-Blant, P., & Forveille, T. 2021, A&A, 646, A59
Schütz, O., Meeus, G., & Sterzik, M. F. 2005, A&A, 431, 165
Simon, J. B., Hughes, A. M., Flaherty, K. M., Bai, X.-N., & Armitage, P. J. 2015, ApJ, 808, 180
Somigliana, A., Testi, L., Rosotti, G., et al. 2023, ApJL, 954, L13
Speedie, J., & Dong, R. 2022, ApJL, 940, L43
Speedie, J., Dong, R., Hall, C., et al. 2024, Natur, 633, 58
Stadler, J., Benisty, M., Izquierdo, A., et al. 2023, A&A, 670, L1
Stadler, J., Benisty, M., Winter, A. J., et al. 2025, ApJL, 984, L11
Tabone, B., Rosotti, G. P., Cridland, A. J., Armitage, P. J., & Lodato, G. 2022, MNRAS, 512, 2290
Teague, R., Bae, J., Andrews, S. M., et al. 2022, ApJ, 936, 163
Teague, R., Bae, J., & Bergin, E. A. 2019a, Natur, 574, 378
Teague, R., Bae, J., Bergin, E. A., Birnstiel, T., & Foreman-Mackey, D. 2018a, ApJL, 860, L12
Teague, R., Bae, J., Birnstiel, T., & Bergin, E. A. 2018b, ApJ, 868, 113
Teague, R., Bae, J., Huang, J., & Bergin, E. A. 2019b, ApJL, 884, L56
Teague, R., & Foreman-Mackey, D. 2018, RNAAS, 2, 173
Teague, R., Guilloteau, S., Semenov, D., et al. 2016, A&A, 592, A49
Teague, R., Henning, T., Guilloteau, S., et al. 2018c, ApJ, 864, 133
Teague, R., Jankovic, M. R., Haworth, T. J., Qi, C., & Ilee, J. D. 2020, MNRAS, 495, 451
Teague, R., Law, C., Huang, J., & Meng, F. 2021, JOSS, 6, 3827
Trapman, L., Longarini, C., Rosotti, G., et al. 2025, ApJL, 984, L18
Veronesi, B., Longarini, C., Lodato, G., et al. 2024, A&A, 688, A136
Veronesi, B., Paneque-Carreño, T., Lodato, G., et al. 2021, ApJL, 914, L27
Villenave, M., Ménard, F., Dent, W. R. F., et al. 2020, A&A, 642, A164
Weaver, E., Isella, A., & Boehler, Y. 2018, ApJ, 853, 113
Wichmann, R., Covino, E., Alcalá, J. M., et al. 1999, MNRAS, 307, 909
Wolff, S. G., Perrin, M., Millar-Blanchaer, M. A., et al. 2016, ApJL, 818, L15
Wölfer, L., Barraza-Alfaro, M., Teague, R., et al. 2025, ApJL, 984, L22
Yoshida, C. T., Curone, P., Stadler, J., et al. 2025, ApJL, 984, L19
Yoshida, T. C., Nomura, H., Tsukagoshi, T., Furuya, K., & Ueda, T. 2022, ApJL, 937, L14
Yu, H., Teague, R., Bae, J., & Öberg, K. 2021, ApJL, 920, L33
Zawadzki, B., Czekala, I., Galloway-Sprietsma, M., et al. 2025, ApJL, 984, L14
Zhang, K., Bergin, E. A., Blake, G. A., Cleeves, L. I., & Schwarz, K. R. 2017, NatAs, 1, 0130
Zhou, Y., Bowler, B. P., Yang, H., et al. 2023, AJ, 166, 220
Zhu, Z., Andrews, S. M., & Isella, A. 2018, MNRAS, 479, 1850